Numerical Weather Prediction

Standard test results for a shallow water model
on the Fibonacci Grid

Forecasting Research Technical Report No. 480

Richard Swinbank (Met Office) and R.James Purser (NCEP and SAIC)

May 2006

email: nwp_publications@metoffice.gov.uk

Document review history

Title: Standard test results for a shallow water model on the Fibonacci Grid
Authors: Richard Swinbank and Jim Purser

Date	Version	Action/comments:	Approval
2/5/06	1	New report combining section 4 of Fibonacci_combined_v9.doc with notes of additional tests carried out for revision of paper.	
2/5/06	1	Approved for issue as Technical Report	A.C. Lorenc
4/5/06	1	Final amendments for issue as FRTR480	
17/5/06	1	Change format of review history	

Standard test results for a shallow water model on the Fibonacci Grid

by Richard Swinbank and R James Purser (NCEP / SAIC)

Abstract

Swinbank and Purser (1999, 2006) introduced a novel framework for global numerical models, named the "Fibonacci Grid". Those papers describe the construction of a model of the shallow-water equations, based on fourth-order accurate finite differences on the Fibonacci Grid. The current report summarises the results from a suite of test cases for shallow water models that were defined in detail by Williamson *et al.* (1992), and is an expanded version of section 4 of Swinbank and Purser (2006).

Introduction

Swinbank and Purser (1999, 2006) introduced a novel method to cover a sphere with a set of points that are geometrically regular and essentially uniformly distributed. The algorithm to generate this set of grid-points is based on Fibonacci numbers, and consequently this type of grid is referred to as a Fibonacci Grid. By building a model of the shallow-water equations using this framework, Swinbank and Purser (2006) demonstrated that this grid could be used as a framework for global atmospheric models. That paper described the geometrical properties of the Fibonacci Grid and the construction of a model of the global shallow-water equations, based on fourth-order accurate spatial finite differences and using a fourth-order Runge-Kutta time integration scheme.

In order to make an assessment of the performance of the shallow-water model, we have carried out some of the standard tests defined by Williamson *et al.* (1992). First, we have tested the advection scheme of the model in isolation, by advecting a cosine bell pattern with a constant, specified wind field. Secondly, we have carried out several of the standard test cases for the full shallow-water model equations. Those tests include: global steady-state nonlinear geostrophic flow; zonal flow over an isolated mountain; and the evolution of a zonal wavenumber-four Rossby-Haurwitz wave. A summary of some test results were presented by Swinbank and Purser (2006), but we present a fuller set of results here. The test cases are referred to using the case numbers referred to by Williamson *et al.* (1992); the reader is referred to that paper for the precise definitions and parameter settings.

For this paper, we present results produced at medium resolution (N=5000, grid-length approximately 226 km) and at high resolution (N=20000, grid-length approximately 113 km). (N refers to the number of grid points in each hemisphere; the grid points are numbered from $-N$ to $+N$, i.e., there are $2N+1$ grid points altogether). The most important model parameters for each resolution are summarised in Table 1. The results presented here are all produced using fourth-order accurate horizontal differencing both for the normal zone-differencing and over the polar caps. Some of the tests were performed using both second-order and fourth-order accurate spatial differencing. Experiments showed that the second-order accurate version of the model was more numerically stable than the fourth-order

version. However, the fourth-order solutions were superior, and we only show those results in this paper.

Table 1

Fibonacci Model Parameters

Resolution	N=5000 (low diffusion)	N=5000	N=20000
Nominal grid length (√A)	225.8 km	225.8 km	112.9 km
Timestep	15 min	15 min	7.5 min
Diffusion filter dilution factor	0.0833	1.0	1.0

Case 1: Advection of a Cosine Bell

In this set of tests a cosine bell is advected once around the sphere, using a specified wind field that corresponds to solid body rotation. The magnitude of the wind is chosen so that after 12 days the solution should exactly overlay the initial data. Several orientations of the advecting wind are specified: around the equator, directly over the poles and minor shifts from these two orientations. The orientations are specified using a parameter α, which is that angle between the axis of solid body rotation and the polar axis. We have run tests with α=0.0, -0.05, +0.05, π/2, π/2-0.05, π/2+0.05. The values of α that are additional to those specified by Williamson *et al.* (α=-0.05, π/2+0.05) were included because the chirality of the Fibonacci grid means that those solutions are not just reflections of the solutions for α=+0.05 and α= π/2-0.05.

Figure 1 shows the advection results for the six different orientations. In each case, the initial position of the cosine bell coincides closely with the position after the shape is advected completely around the globe. There is a slight spreading of the bell shape over the 12-day period, as a result of the diffusion applied in the model. The six plots look essentially indistinguishable, so later results from the advection tests are only plotted for α= π/2, where the advection was over the poles. All the model results are plotted by interpolating from the model grid to a one-degree resolution latitude-longitude grid. Since that resolution is finer than the model resolutions we have used, any structures on the model grid-scale will be visible in the plotted maps.

In order to run the full shallow-water model, it proved necessary to run with rather higher diffusion settings. Figure 2(a) shows the result of the advection with low diffusion and *N*=5000 (as Fig. 1), while Fig. 2(b) shows the advection tests with diffusion settings as required by the full model. In that case, the diffusion has smoothed out the cosine bell much more strongly, although its position is still in very good agreement with its starting location. Figure 2(c) shows the advection results with *N*=20000, again with diffusion setting used in the full model. In that case, the finer grid means that the diffusion is having much less effect, and results are essentially the same as for *N*=5000, with low diffusion.

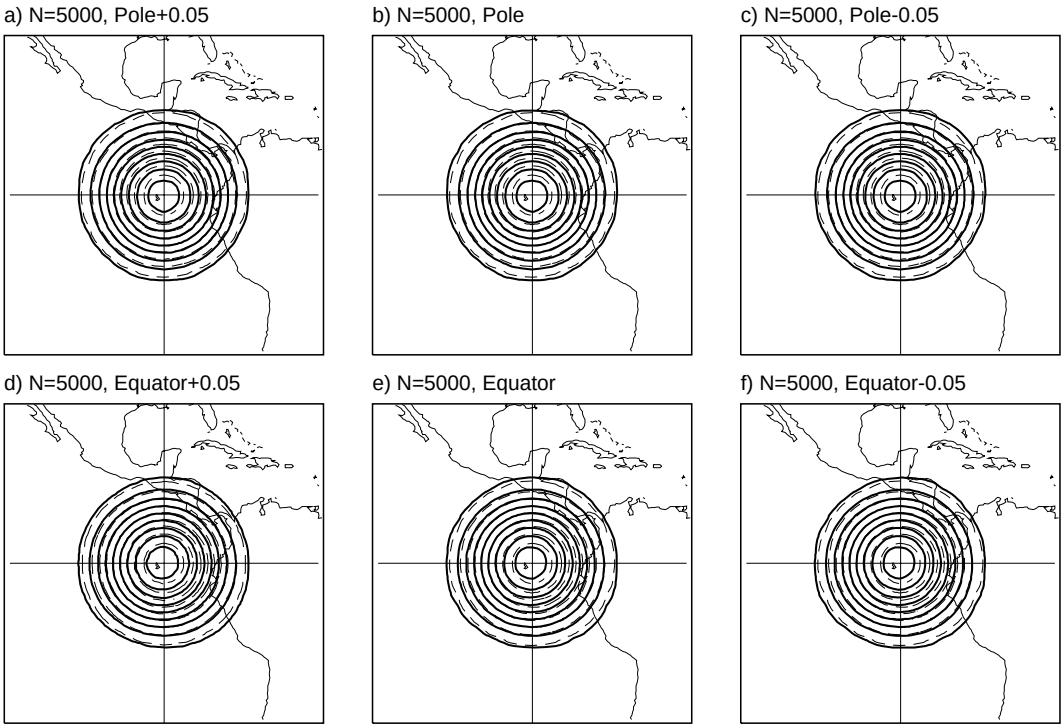

Figure 1: Results of polar advection test for *N*=5000, with varying values of α: a) π/2+0.05, b) π/2, c) π/2-0.05, d) +0.05, e) 0.0, f) -0.05. The dashed lines show the initial location of the cosine bell, and the full lines the final location, which should coincide exactly.

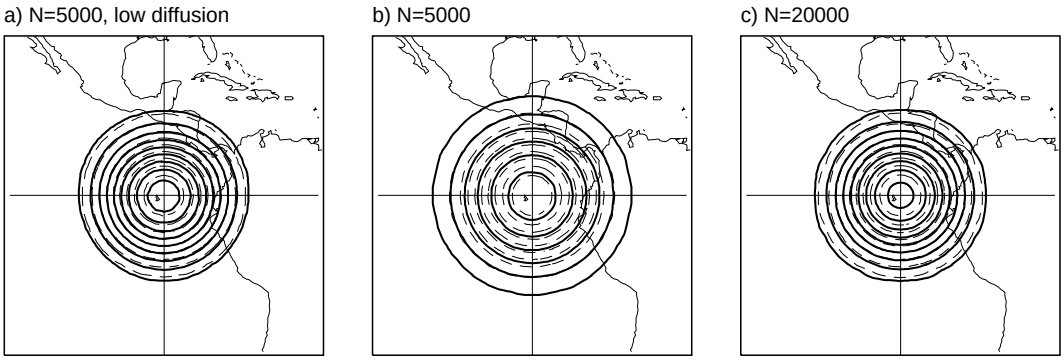

Figure 2: Results of polar advection test at a) *N*=5000 and low diffusion (same as Fig. 1b), b) *N*=5000, c) *N*=20000.

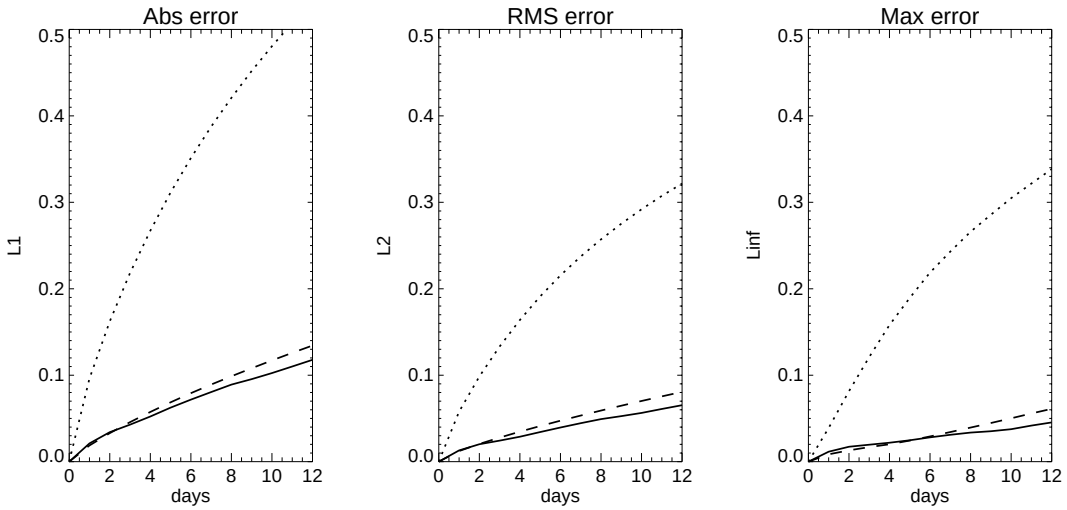

Figure 3: Statistical comparisons between polar advection test results and the true solution. Statistics L_1, L_2 and L_∞ are plotted daily from day 0 to day 12, through a complete revolution. Solid line – N=5000, low diffusion; dotted line – N=5000, with diffusion as in full model; dashed line – N=20000, with diffusion as in full model.

Figure 3 shows statistical comparisons of the advection results with the true solution. We plot time series of the normalized absolute, root mean square and maximum differences, in terms of the L_1, L_2 and L_∞ diagnostics defined by Williamson *et al* (1992). These statistics are calculated from the output fields on the original model grid, assuming that each grid point represents the same area, i.e., there is no area-weighting in the calculations. (As shown by Swinbank and Purser, 2006, this is a very good approximation.) Figure 3 demonstrates that the error statistics grow quickly from the beginning of the integrations, as one would anticipate from errors dominated by diffusion.

In summary, the results show that the advective processes are treated well on the Fibonacci Grid. However, the steep gradients in the cosine bell pattern make it susceptible to the diffusive filtering.

Case 2: Steady nonlinear geostrophic flow

This case is a steady state solution to the non-linear shallow water equations. It consists of a solid body rotation in balance with the corresponding geopotential height field. As in the previous test, Williamson et al (1992) specify a number of different orientations, in which the Coriolis parameter is a function of both latitude and longitude, i.e., the earth's rotation axis does not necessarily coincide with the axis of the model grid. Since these unconventional orientations would have entailed major recoding of the model, the case has only been run with α=0.0. Results from case 1 suggest that the model results are not sensitive to the grid orientation, so we would not expect results of tests with different values of α to differ significantly from those presented here.

Plots of the height and wind fields (not shown) demonstrated that the flow was stable over the integration period (15 days), with little visible change. Since the result should be a steady state solution, error diagnostics were calculated by comparing the flow during the integration with the initial data. Figure 4 shows time series of the L_1,

L_2 and L_∞ diagnostics; as in case 1, these statistics are calculated on the original model grid. They all show a roughly linear increase with time; within the 15 day period of the run the errors remain small.

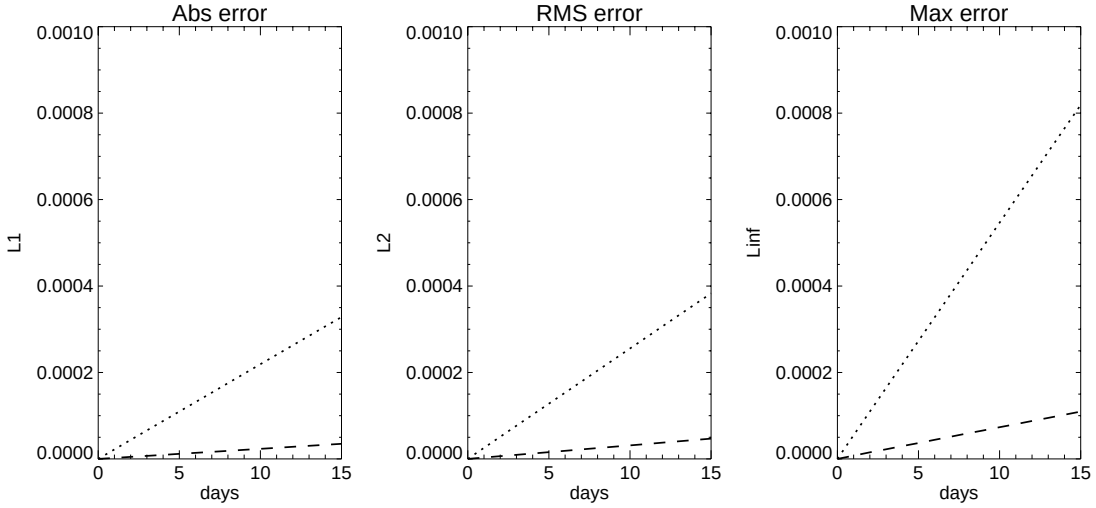

Figure 4: Statistical comparisons between height field and the true solution for the case of steady geostrophic flow. Statistics L_1, L_2 and L_∞ are plotted daily from day 0 to day 15. Here, and in subsequent time series, the dotted lines show results for N=5000, and dashed for N=20000.

Case 5: Zonal flow over an isolated mountain

In this case the initial wind and height field are exactly the same as for case 2, but an isolated conical mountain was imposed, centred at latitude $\pi/6$ and longitude $3\pi/2$. In order to run this test, the model was recoded to allow for non-zero orography. The main aim of this test is to check for integral invariants, i.e. to check how much the total mass, energy and potential enstrophy vary during the integration. Since an analytical solution is not known, Williamson *et al* have provided a reference solution, for comparison purposes.

The case was run for 15 days. Figure 5 shows the simulated model height fields from run at N=20000, at days 5 and 15. The results appear very similar to the supplied reference solution; this is demonstrated with the difference fields that are also plotted in Fig. 5. Apart from differences resulting from interpolation errors in the vicinity of the mountain, there is a set of wave-like differences that originate near the mountain and propagate around the globe during the integration; a qualitatively similar feature was also found by Thuburn (1997).

In this case, the error statistics were calculated from the data interpolated to a 1° latitude-longitude grid, rather than the original model grid points, in order to make it simpler to compare the results to the supplied reference solution. The "error" diagnostics (Fig. 6) show differences compared with the supplied reference solution. Further inspection shows that the large maximum (L_∞) errors result from interpolation errors around the mountain, where the slope changes very sharply. This is the only plot that appears materially affected by our calculating the error statistics on a 1° grid rather than the model grid.

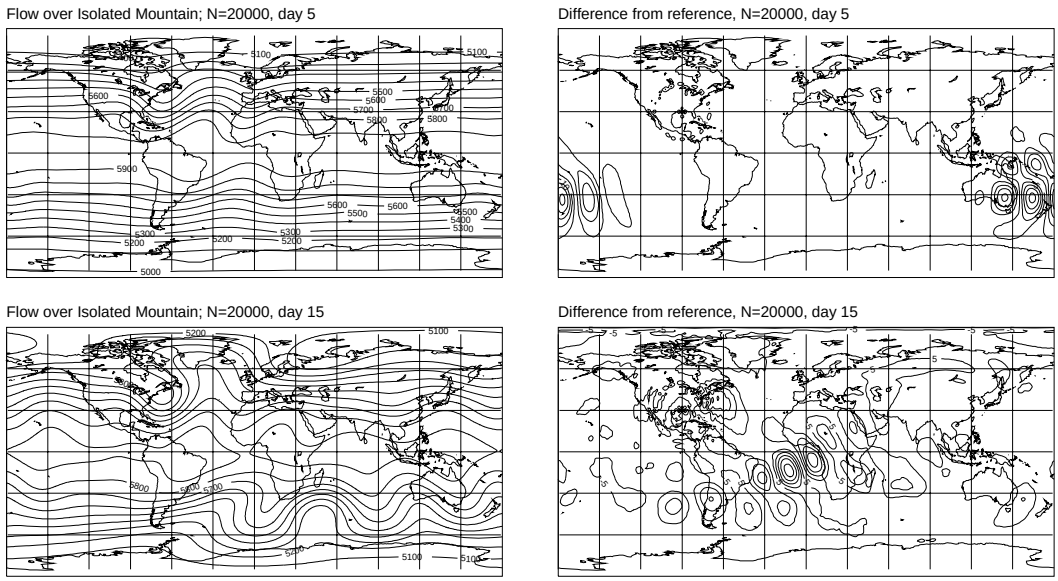

Figure 5: The evolution of height fields for the case of zonal flow over an isolated mountain: a) simulation after 5 days (contour interval 100m), b) difference from reference solution after 5 days (contours interval 5m, omitting zero contour) c) and d) as a) and b) respectively, but after 15 days.

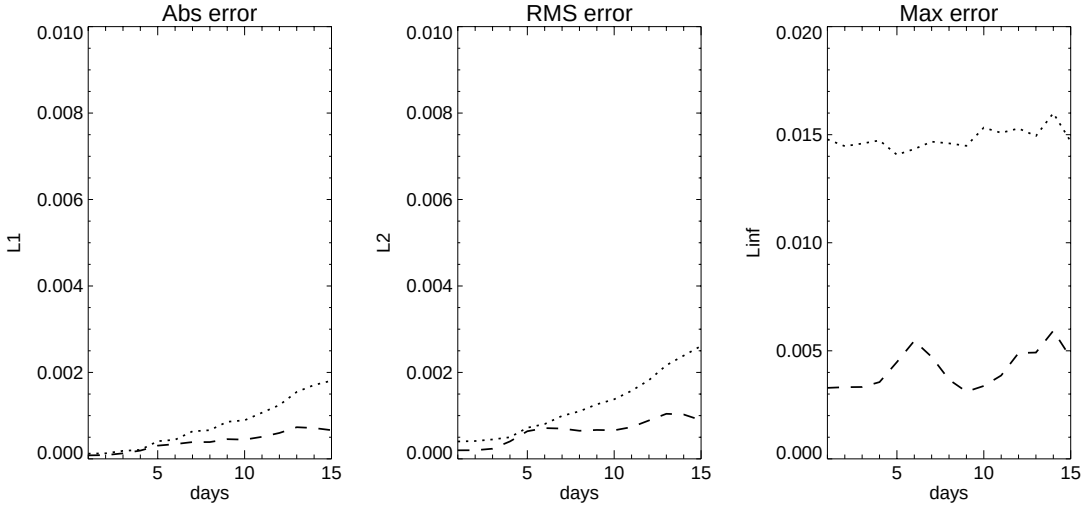

Figure 6: Statistical comparisons between height field and the supplied reference solution for the case of zonal flow over an isolated mountain. Statistics L_1, L_2 and L_∞ are plotted daily from day 0 to day 15.

Figure 7 shows time series of three global invariants: total mass, total energy and potential enstrophy. While the conservation of total mass is not enforced in the model, the statistics indicate that it is not a major problem; the total mass has changed by around 1 part in 10^5 after 15 days at N=5000, and an order of magnitude less at N=20000. Time series of the energy and potential enstrophy show significant decreases through the 14-day integration period, probably reflecting the strong diffusion.

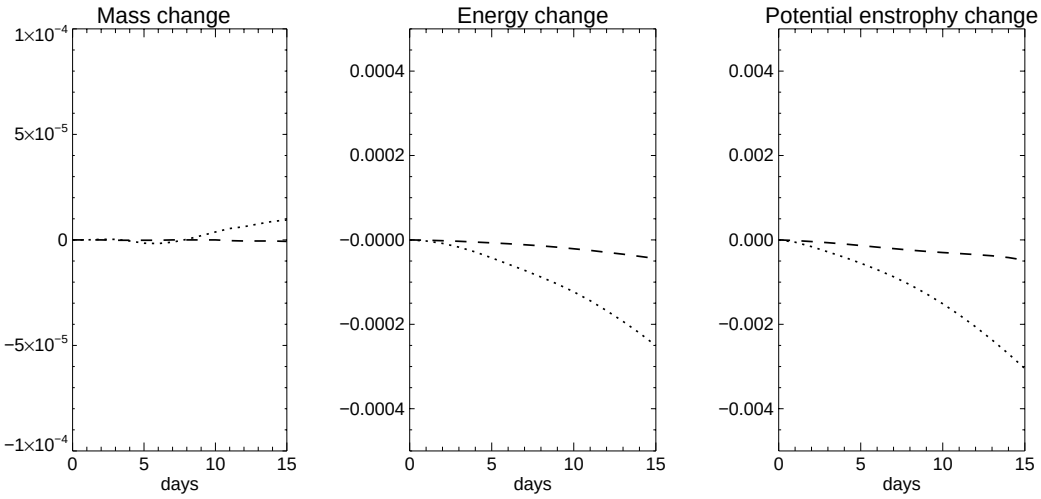

Figure 7: Global invariants for the case of zonal flow over an isolated mountain. The graphs show relative changes to the total mass, energy and potential enstrophy.

Case 6: Rossby-Haurwitz wave

Another test commonly applied to shallow-water models is the simulation of Rossby-Haurwitz waves. The initial height and velocity fields are defined by analytic functions of latitude, longitude and various wave parameters. In a non-divergent barotropic model the wave pattern moves eastward without changing shape. While the Rossby-Haurwitz waves are not analytic solutions of the shallow-water equations, they evolve in a somewhat similar manner, progressing eastward with some change of shape. Since the true solution is not known, we have again compared our results with the reference solution from Williamson *et al.* (1992).

The Rossby-Haurwitz wave tests have been run at both medium (N=5000) and high (N=20000) resolution, each for a 14-day period. Figure 8 shows the starting conditions (day 0) and results at day 14 from the two Fibonacci shallow-water model runs, along with the day 14 reference solution. The medium-resolution results (Fig. 8(c)) are essentially in phase with the reference solution (Fig. 8(b)), but the shape of the waves has changed significantly. The troughs have become more intense and the ridges have become narrower, coupled with an increase in heights at high latitudes. The waves have acquired a noticeable poleward-westward tilt. This tilt is evidence of vacillations in wave structure that have also been found in solutions from other numerical models (see Thuburn and Li, 2000). There is a degree of asymmetry between the solutions in the two hemispheres that results from the chirality of the model grid. There are other small asymmetries between individual waves within a hemisphere, which result from the asymmetric nature of the grid. At high resolution (N=20000, Fig. 8(d)), the overall shape of the wave is closer to the reference solution, and the initial conditions, indicating the improved accuracy resulting from better resolution.

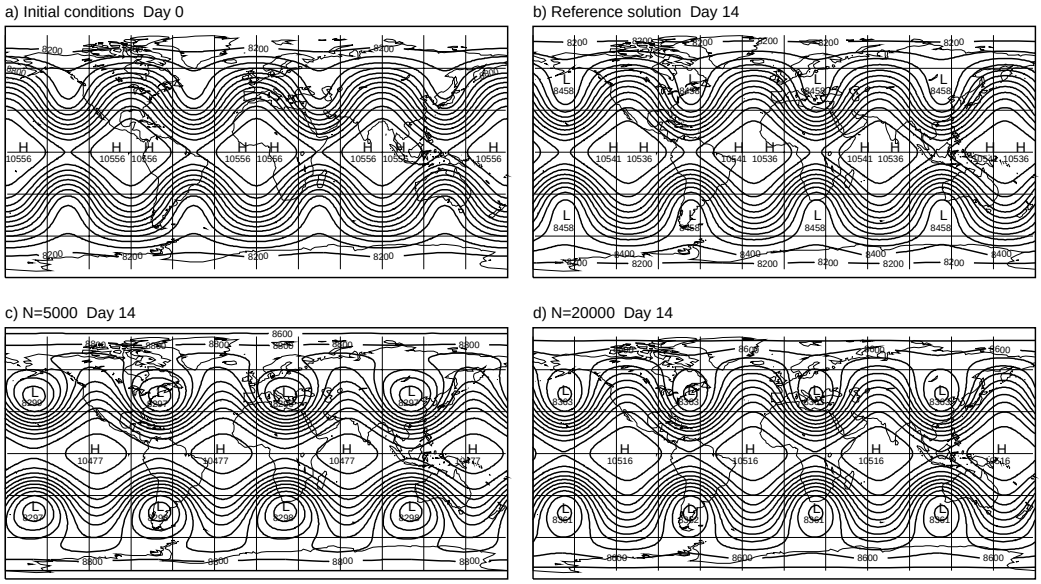

Figure 8: Height fields from simulations of the Rossby-Haurwitz wave (contour interval 200m): a) initial conditions, day 0; b) day 14 from the reference solution; c) day14, simulation using N=5000; d) day 14, simulation using N=20000.

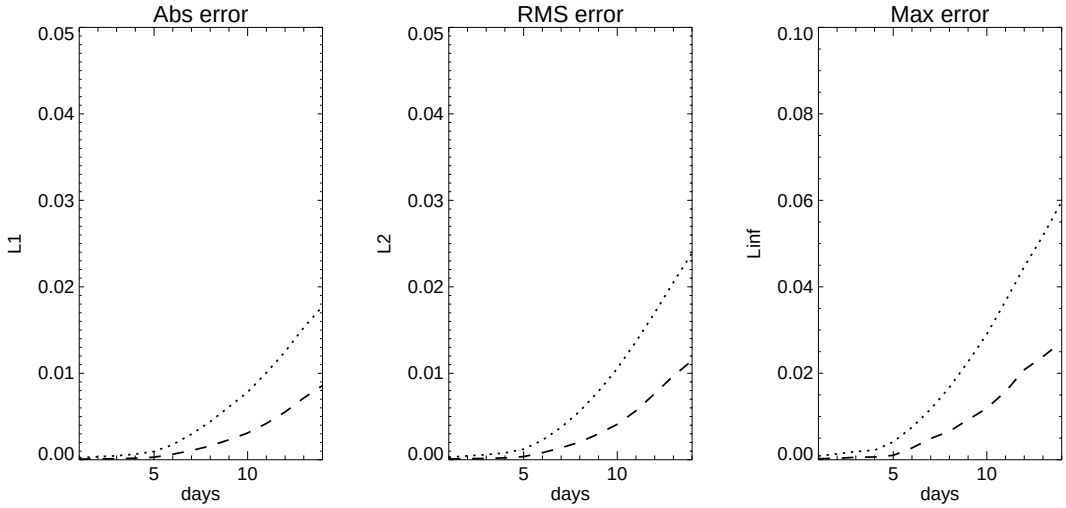

Figure 9: Statistics L_1, L_2 and L_∞ for Rossby-Haurwitz wave simulations, compared with the reference solution for days 1 to 14.

Figure 9 quantifies the errors from the two model runs; as in case 5, statistics were calculated using a 1° grid. In this case, the errors grow relatively slowly at the start, as the solutions gradually diverge. This indicates that, for this test, the errors are not so dominated by the diffusion. The normalized errors L_1, L_2 and L_∞ errors are much smaller than in the advection test, and probably more indicative of values obtainable in real-life situations.

The time series of the total mass (Fig. 10) shows a similar magnitude change to that found for case 5. Time series of the energy and potential enstrophy show stronger decreases through the 14-day integration period (by 0.15% and 2%

respectively at N=5000), indicating that the Rossby-Haurwitz wave is a more sensitive test for those invariants than the flow over the isolated mountain.

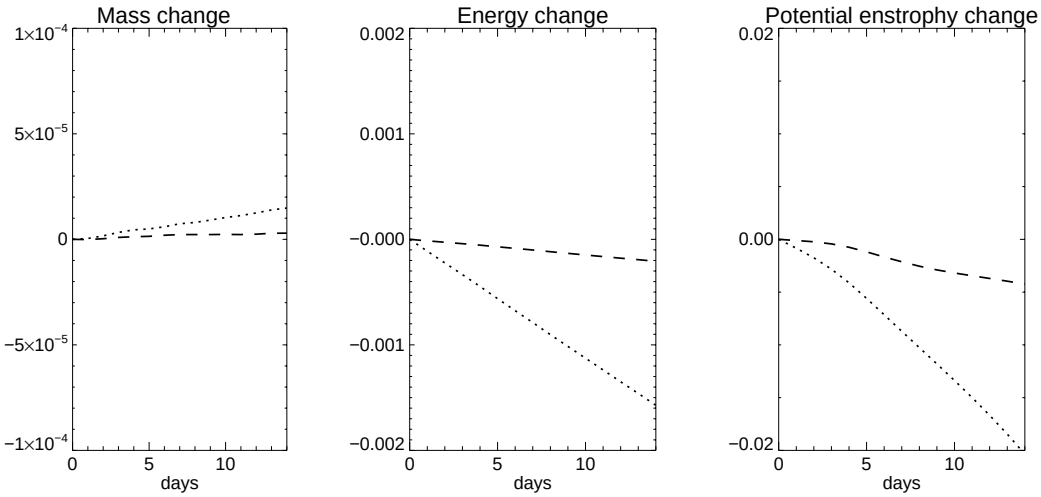

Figure 10: Invariant statistics for Rossby-Haurwitz wave simulations.

Conclusions

We have presented results from a shallow-water equation model based on the Fibonacci Grid framework. The results demonstrate that it is feasible to build a shallow-water model using the Fibonacci Grid framework. The first test shows that the Fibonacci Grid framework allows accurate advection results. Although the model is not formulated to enforce conservation of mass, this does not appear to be a major issue. However, the high diffusion required to run the full Eulerian shallow-water model demonstrates that the current model has limitations. In particular, the results show that there is a significant decrease in total energy and potential enstrophy.

As outlined by Swinbank and Purser (2006), there are a number of avenues that could be explored to develop a model on the Fibonacci grid that could potentially perform better. The current framework may be used for higher-order finite difference schemes. Other possible developments include the construction of a semi-Lagrangian model, a finite element model or the use of Arakawa-type finite difference schemes that would conserve enstrophy and energy. The current results are only a first step towards the exploitation of the remarkable geometry of the Fibonacci grid.

Acknowledgements: We thank one of the referees of Swinbank and Purser (2006) for encouraging us to carry out a more complete set of tests and John Truesdale for help with the shallow-water model reference solutions.

References

Swinbank, R. and R.J. Purser, 1999: Fibonacci Grids. *Preprints of the 13th conference on Numerical Weather Prediction*, (Denver, 13-17 September 1999), American Meteorological Society, 125-128.

Swinbank, R. and R.J. Purser, 2006: 'Fibonacci Grids: a novel approach to Global Modelling', *Quart. J. R. Met. Soc.,* in press.

Thuburn, J., 1997: A PV-based shallow-water model on a hexagonal-icosahedral grid. *Mon. Wea. Rev.*, **125**, 2328-2347.

Thuburn, J. and Y. Li, 2000: Numerical simulations of Rossby-Haurwitz waves. *Tellus A*, **52**, 181-189.

Williamson, D.L, J.B. Drake, J.J. Hack, R. Jakob and P.N. Swarztrauber, 1992: A standard test set for numerical approximations to the shallow water equations in spherical geometry. *J. Comp. Phys.*, **102**, 211-224.